



Selective Naked-Eye Detection of SARS-CoV-2 Mediated by N Gene Targeted Antisense Oligonucleotide Capped Plasmonic Nanoparticles

Parikshit Moitra,[#] Maha Alafeef,[#] Ketan Dighe, Matthew B. Frieman, and Dipanjan Pan^{*}



Cite This: <https://dx.doi.org/10.1021/acsnano.0c03822>



Read Online

ACCESS |

Metrics & More



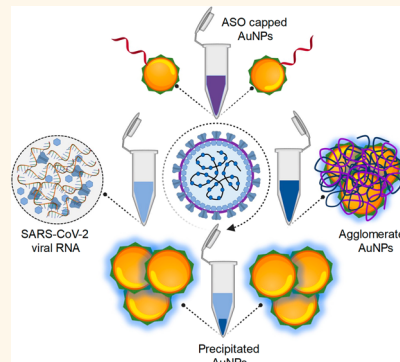
Article Recommendations



Supporting Information

ABSTRACT: The current outbreak of the pandemic coronavirus disease 2019 (COVID-19) caused by the severe acute respiratory syndrome-coronavirus-2 (SARS-CoV-2) demands its rapid, convenient, and large-scale diagnosis to downregulate its spread within as well as across the communities. But the reliability, reproducibility, and selectivity of majority of such diagnostic tests fail when they are tested either to a viral load at its early representation or to a viral gene mutated during its current spread. In this regard, a selective “naked-eye” detection of SARS-CoV-2 is highly desirable, which can be tested without accessing any advanced instrumental techniques. We herein report the development of a colorimetric assay based on gold nanoparticles (AuNPs), when capped with suitably designed thiol-modified antisense oligonucleotides (ASOs) specific for N-gene (nucleocapsid phosphoprotein) of SARS-CoV-2, could be used for diagnosing positive COVID-19 cases within 10 min from the isolated RNA samples. The thiol-modified ASO-capped AuNPs agglomerate selectively in the presence of its target RNA sequence of SARS-CoV-2 and demonstrate a change in its surface plasmon resonance. Further, the addition of RNaseH cleaves the RNA strand from the RNA–DNA hybrid leading to a visually detectable precipitate from the solution mediated by the additional agglomeration among the AuNPs. The selectivity of the assay has been monitored in the presence of MERS-CoV viral RNA with a limit of detection of 0.18 ng/ μ L of RNA having SARS-CoV-2 viral load. Thus, the current study reports a selective and visual “naked-eye” detection of COVID-19 causative virus, SARS-CoV-2, without the requirement of any sophisticated instrumental techniques.

KEYWORDS: gold nanoparticle, naked-eye detection, COVID-19, antisense oligonucleotide, hyperspectral imaging, SARS-CoV-2



An unexpected outbreak of coronavirus disease 2019 (COVID-19) has collapsed many health care systems and crashed numerous economies. The disease was first identified in December 2019 and has since rapidly spread across the world, resulting in the ongoing 2019–20 pandemic.¹ It has filled hospitals and emptied public spaces while disrupting a modern society on a scale that most people in the world have never witnessed in their lifetime.^{2–4} Like most of the previous modern epidemics and pandemics, this newly emerging infectious disease is caused by the novel severe acute respiratory syndrome-coronavirus-2 (SARS-CoV-2) virus.^{5,6} The COVID-19 pandemic is believed to have close similarities with severe acute respiratory syndrome (SARS) and the Middle East respiratory syndrome (MERS) in terms of causing severe acute respiratory distress.^{7,8} An average of two or three people are getting infected from every already affected person because of the higher transmission rate for COVID-19.^{9–11}

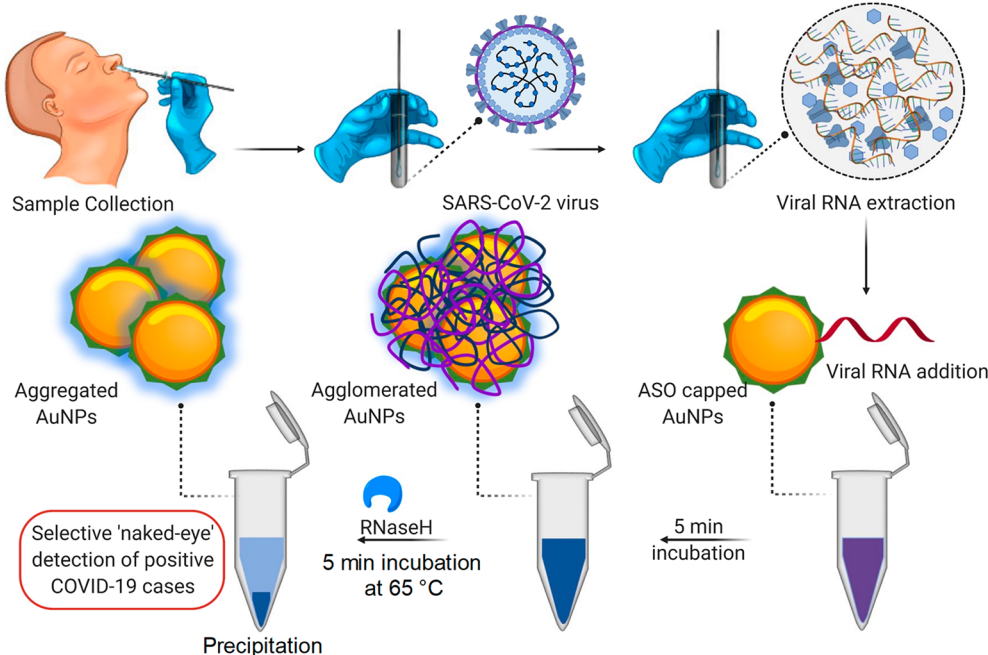
The efforts to contain the virus are ongoing, but considering the many uncertainties regarding the pathogen transmissibility and virulence the efficacy of these efforts is unknown. A crucial shortcoming of the healthcare systems across the globe has been the ability to rapidly and accurately diagnose the disease with contributing factors that include a shortage of test kits and specimen materials, availability of personal protective equipment and reagents, limited certified testing centers, and no established funding mechanism to support these testing

Received: May 7, 2020

Accepted: May 21, 2020

Published: May 21, 2020

Scheme 1. Schematic Representation for the Selective Naked-Eye Detection of SARS-CoV-2 RNA Mediated by the Suitably Designed ASO-Capped AuNPs



facilities.¹² Further, the lack of rapid diagnostic tests along with the inaccessibility of the advanced instrumental techniques to all the diagnostic centers, especially the remote ones, contribute to the confusion surrounding which individuals should be quarantined, limit epidemiological data, and the ability to track pathogen transmission within as well as across communities. Therefore, a key part for the management of COVID-19 pandemic lies in “flattening the curve”, that is, decreasing the epidemic peak, through different measures taken for reducing the rate of new infections.^{13,14}

The ability to perform pervasive testing has already shown benefits to countries such as South Korea and Singapore,^{15,16} providing precise information about mandatory quarantine for a carrier of the virus and rigorous contact tracing which in turn results in greater control in slowing the spread of the disease. Downmodulating the infection rate will therefore help to minimize the risk of overwhelming health facilities, allowing faster care of existing cases and delaying new cases before therapeutics or a vaccine are available.^{17–20} At present, COVID-19 is being primarily diagnosed by three techniques: (1) reverse-transcription polymerase chain reaction (RT-PCR) and gene sequencing; (2) a lateral flow immunoassay, which is a common point-of-care (POC) diagnostic approach that detects antibodies against SARS-CoV-2 in patient samples; and (3) chest computed tomography (CT). Out of these, chest CT has been identified as a major screening tool, if available.^{21,22} Moreover, the current gold standard approach for screening COVID-19 requires access to reverse transcriptase real-time PCR assay (RT-PCR), which can be carried out using a variety of clinical specimens, including blood, feces, bronchoalveolar lavage fluid, sputum, fiber bronchoscope brush biopsies, nasal swabs, or pharyngeal swabs.^{23,24} On the basis of this technique, numerous laboratories have developed experimental protocols using quantitative RT-PCR (qRT-PCR) methods for virus identification within 4–6 h, including a test developed by U.S. Centers for Disease Control and Prevention (CDC) and approved under emergency use authorization (EUA) proc-

ess.²⁵ However, limitations of sample collection and transportation, as well as the performance of the kit with inadequate access to advanced instrumental techniques, often cannot report positive COVID-19 cases at its initial presentation leading to the spread of this infectious disease to a wider community. Furthermore, traveling to a clinical setting for testing increases the risk of spreading the SARS-CoV-2 virus which further adds strain to a resource-limited healthcare system. Additionally, while serological tests are rapid, POC, and require minimal equipment, their efficacy may be limited in the diagnosis of acute SARS-CoV-2 infection only, as it may take several days to weeks after the onset of the symptom for a patient to develop a detectable antibody response.²⁶ Therefore, as some of the existing techniques remain laborious and technically challenging, there is an urgent unmet need for a POC, rapid, cost-effective, and selective diagnostic test for COVID-19 that can provide fast and accurate test results within a duration of less than an hour and possibly within minutes.²⁷

Nanotechnology-based colorimetric bioassays are convenient and attractive in biosensor design for their simplicity, visual output, and no necessity for complex instruments.^{28–32} In recent years, gold nanoparticle (AuNPs) have garnered incredible attention in the field of colorimetric-based biosensing applications due to their exceptional optical properties such as high extinction coefficient, localized surface plasmon resonance, and inherent photostability.^{33,34} They have been utilized in numerous colorimetric-based biosensing applications to detect a wide range of chemical and biological targets like small molecules, proteins, metal ions, and nucleic acids where the particle changes its color in response to the reactivity of the nanosized particles to the external conditions.^{35–43} Despite these features, however, this technique still involves the preparation of ssDNA probes and the implementation of several intermediate steps, such as time-intensive denaturation and annealing after PCR.⁴⁴ Furthermore, given that both ssDNA and dsDNA stabilize the AuNPs

Table 1. Selected ASO Sequences Targeted for the N-Gene of SARS-CoV-2

starting target position	ending target position	target sequence (5p → 3p)	antisense oligo (5p → 3p)	GC content	binding site disruption energy (kcal/mol)	binding energy (kcal/mol)
421	440	ACACCAAAAGAUCAUCAUUGG	CCAATGTGATCTTTGGTGT (ASO1)	40.0%	7.6	-15.8
443	462	CCCGCAAUCCUGCUAACAAU	ATTGTTAGCAGGATTGCGGG (ASO2)	50.0%	7.6	-10.4
836	855	CAGAACAAACCCAAGGAAAU	ATTCCCTGGGTTTGTCTG (ASO3)	40.0%	6.0	-14.3
886	905	ACUGAUUACAAACAUUGGCC	GGCCAATGTTGTAATCAGT (ASO4)	40.0%	8.7	-10.0

at low salt concentrations, cationic agents are primarily required to detect the target with probes. A colorimetric bioassay was thus developed for the detection of DNA/RNA targets based on unmodified AuNP aggregation using disulfide self-assembly of terminal modified DNA.⁴⁵ The products generated in this approach not only demonstrated a high affinity for the surface of AuNPs but also protected them efficiently from salt-induced aggregation. Additionally, a colorimetric assay based on a similar approach was also reported to detect the presence of Middle East respiratory syndrome coronavirus (MERS-CoV).⁴⁶

Accordingly, we realized the importance of nanotechnology in controlling the spread of COVID-19^{47–49} and utilized its exclusive features in developing a colorimetric assay based on AuNPs. These AuNPs, when capped with suitably designed thiol-modified antisense oligonucleotides (ASOs) specific for N-gene (nucleocapsid phosphoprotein) of SARS-CoV-2, could potentially be used for diagnosing positive COVID-19 cases within a few minutes. The methodology, described herein, utilizes an all-inclusive targeting approach mediated by four of the ASO sequences covering two regions of the viral N-gene sequence at the same time. These thiolated ASO-capped AuNPs agglomerate only in the presence of its target RNA sequence of SARS-CoV-2 and thus demonstrate a change in its surface plasmon resonance (SPR), which is further amplified with the addition of RNaseH leading to the visually detectable precipitation of gold nanoparticles (Scheme 1). The agglomeration of ASO-capped gold nanoparticles in the presence of SARS-CoV-2 RNA was studied by UV-visible absorbance spectroscopy, transmission electron microscopy (TEM), and enhanced dark-field hyperspectral imaging technique. Thus, the current study utilizes the intrinsic optical properties of plasmonic AuNPs and targeting ability of the ASOs to develop a selective, and “naked-eye” detection platform for the current COVID-19 causative virus, SARS-CoV-2, without the requirement of any expensive instrumental techniques. The reliability and reproducibility of the current biosensor increases based on its design of simultaneous targeting of two of the N-gene regions of SARS-CoV-2, ensuring the feasibility of the assay even if one region of the viral gene undergoes mutation during its current spread.

RESULTS AND DISCUSSION

Strategy Behind the Sensor Development. During the current spread of COVID-19 causative virus, SARS-CoV-2, scientists have discovered three regions among the SARS-related viral genomes that had conserved sequences. These sequences are (a) RdRP gene (RNA-dependent RNA polymerase gene) responsible for the open reading frame ORF1ab region, (b) E gene (envelope protein gene), and (c) N gene (nucleocapsid phosphoprotein gene).²⁸ The analytical sensi-

tivity of both the *RdRP* and *E* genes was demonstrated to be quite high (technical limit of detection of 3.6 and 3.9 copies per reaction), while the sensitivity for *N* gene was observed to be weaker (8.3 copies per reaction). This leaves an enormous area for the improvement of biosensors targeted for *N* gene sequence of SARS-CoV-2. Statistically, a sensitive biosensor selectively targeting the *N* gene sequence of SARS-CoV-2 with a visual naked-eye response without the need for access to any sophisticated instrumental techniques would greatly benefit the current sensor development research for COVID-19. In addition to this, the analytical sensitivity of the biosensor can be improved by simultaneous targeting of multiple genetic regions within the same gene sequence, which will add to features of the biosensor. This will also increase the feasibility of the assay even if one region of the viral gene undergoes mutation during its current spread. We therefore targeted *N* gene sequence of SARS-CoV-2 and undertook gold nanoparticle as one of the important anisotropic plasmonic nanostructures for the development of a COVID-19 specific biosensor.³³

Design and Selection of Antisense Oligonucleotides (ASOs). The *N* gene was commenced herein as the target gene sequence for the selective detection of SARS-CoV-2 isolate 2019-nCoV/USA-WA1-A12/2020 (detailed sequence has been provided in the Supporting Information), and a set of ASOs were predicted following a methodology as described in Materials and Methods. Among the predicted ASO sequences, four of the ASOs were selected based on their comparative binding disruption energies and binding energies with the target sequence (Table 1). One of the other parameters behind the selection of these four ASO sequences was their closely following target position. The ASOs were then differentially functionalized: ASO1 and ASO3 were functionalized with thiol moiety at the 5' end, whereas ASO2 and ASO4 were functionalized with thiol moiety at the 3' end (Figure 1a). These ASOs when used to cap gold nanoparticles are expected to become aggregated selectively in the presence of the *N* gene sequence of SARS-CoV-2 which can be corroborated with their complementary binding followed by aggregation propensity among the nanoparticles (Figure 1b).

Standardization of the ASO-Capped AuNPs for the Sensitive Detection of SARS-CoV-2. Accordingly, the differentially functionalized thiol-modified ASOs were utilized to exchange the surface capping agent of the citrate stabilized gold nanoparticles. The TEM images (Figure 2a,b) show that the ASO-capped AuNPs are individually dispersed with no visible aggregation. All of the four ASO-capped AuNPs exhibit a small anhydrous size of <30 nm, which are well dispersed without the formation of a large entity. Figure 2c shows the average hydrodynamic sizes of the four individual ASO-capped gold nanoparticles, which were found to be less than 60 nm.

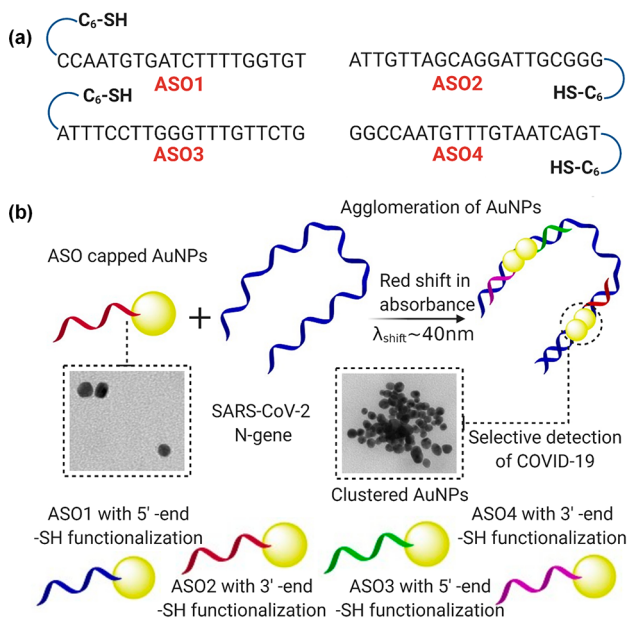


Figure 1. Differentially functionalized ASOs with their sequences are represented in (a). The proposed concept behind the agglomeration of gold nanoparticles, when capped with the ASOs, is schematically presented in (b).

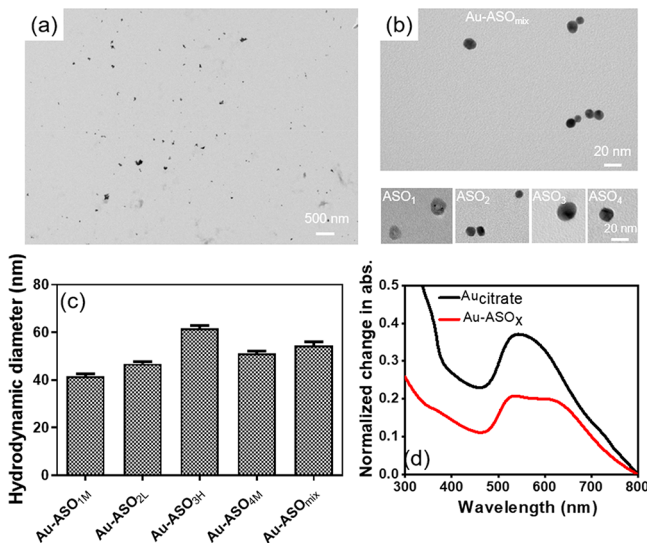


Figure 2. (a) TEM image of ASO-capped gold nanoparticles. (b) Zoomed-in TEM images of Au-ASO_{mix} nanoparticles with the individual ASO-capped AuNPs are shown as insets. (c) Comparative change in hydrodynamic diameter of the gold nanoparticles capped with individual ASOs and the mixture of the four Au-ASOs. Error bar indicates the measurements of hydrodynamic diameter from three such independent experiments. (d) Normalized change in absorbance of the gold nanoparticles before and after the addition of thiol modified ASOs to the citrate stabilized ones.

The formation of ASO-conjugated thiol-stabilized AuNPs was further confirmed from their surface plasmon bands.⁵⁰ Two absorption peaks, one at $\sim 530\text{ nm}$ and the other at $\sim 620\text{ nm}$, were observed after the thiol-modified ASO capping on the surface of the AuNPs (Figure 2d).

The relative sensitivity of the various ASO-capped gold nanoparticles toward the target SARS-CoV-2 RNA was then

monitored with the comparative increase in absorbance at 660 nm. It was observed that the surface capping of thiol-modified ASOs together with the comparative ratio of the ASOs to the AuNPs (ASO/AuNPs) play a major role in determining the sensitivity of the gold nanoparticles toward SARS-CoV-2 RNA. To investigate the effect of the ASO/AuNPs ratio on the sensitivity of the sensing platform, three different ratios of ASO/AuNPs have been tested. The ratios are named as the following: high (ASO_H), medium (ASO_M), and low (ASO_L) concentrations for the four ASOs; see Materials and Methods for details. Among these 12 different combinations of the ASO-conjugated AuNPs, which vary in the ratio of ASO/AuNPs, ASO_M was found the most sensitive ratio for the AuNPs capped with ASO1 (i.e., Au-ASO_{1M}). However, among ASO2, the low ratio was found to be the most sensitive in detecting the viral RNA (Au-ASO_{2L}), the high ratio in ASO3 (Au-ASO_{3H}), and finally the medium in ASO4 (Au-ASO_{4M}) (Figure 3).

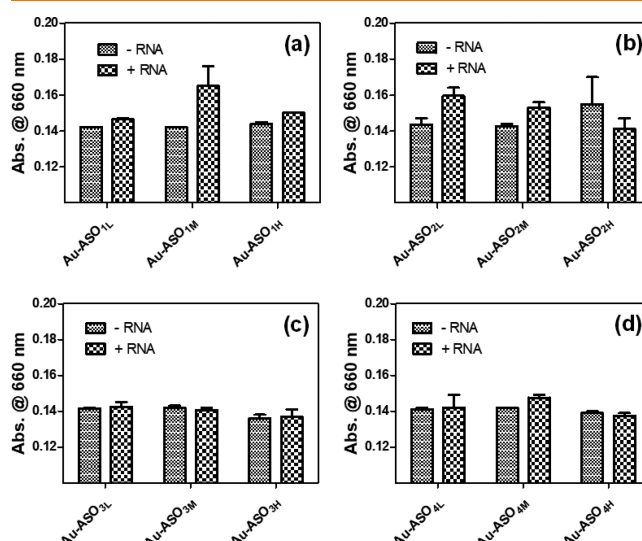


Figure 3. Increase in absorbance at 660 nm for the gold nanoparticles coated with different concentrations of (a) ASO₁, (b) ASO₂, (c) ASO₃, and (d) ASO₄ upon the addition of SARS-CoV-2 RNA. The RNA concentration kept constant at 1 ng/ μL throughout the experiment. The mixture was incubated for 15 min at room temperature prior to recording the change in absorbance in each case. Error bar indicates the average results obtained from three independent experiments performed in triplicate.

After optimizing the ASO to AuNPs ratio to obtain the maximum sensitivity, all four of the ASO-capped AuNPs (i.e., Au-ASO_{1M}, Au-ASO_{2L}, Au-ASO_{3H}, and Au-ASO_{4M}) were mixed (Au-ASO_{mix}) in an equivalent amount with each other to further improve the analytical sensitivity of the gold nanoparticles toward SARS-CoV-2 RNA. Transmission electron microscopy indicated the formation of distinctly dispersed AuNPs (Figure 2b) with the average hydrodynamic diameter of about $55.4 \pm 4.5\text{ nm}$ as observed from Zetaview (Figure 2c and Movie S1). It was expected that the agglomeration propensity among the nanoparticles would increase when treated in a composite manner (Au-ASO_{mix}) with the SARS-CoV-2 RNA. A large redshift of about 40 nm in the aggregation band was also observed when the Au-ASO_{mix} nanoparticles were tested against the SARS-CoV-2 RNA (Figure 4a). The improvement in analytical sensitivity of Au-

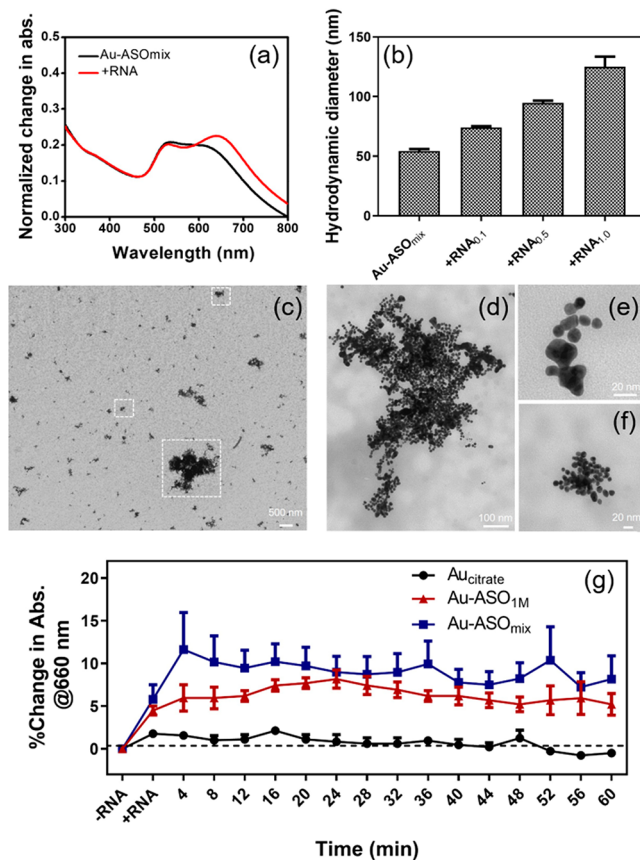


Figure 4. (a) Normalized change in absorbance of the gold nanoparticles before and after the addition of total RNA containing the SARS-CoV-2 viral load. (b) Comparative change in average hydrodynamic diameter of the composite of Au-ASO_{mix} before and after the addition of RNA containing SARS-CoV-2 where the RNA concentration was varied from 0.1 to 0.5 and 1 ng/μL. Error bar indicates the measurements of hydrodynamic diameter from three such independent experiments. (c–f) TEM images of the Au-ASO_{mix} nanoparticles after addition of RNA containing SARS-CoV-2. (g) The percent change in absorbance at 660 nm of the ASO-capped gold nanoparticles at different incubation time points with a definite concentration of 1 ng/μL RNA. Here, the error bar indicates the average results obtained from four such independent experiments performed in triplicates.

ASO_{mix} nanoparticles toward the detection of SARS-CoV-2 viral RNA was further validated by monitoring the relative increase in absorbance at 660 nm in comparison with individual ASO-capped AuNPs (Figure S1). The analytical performance of the sensor was also probed when two of the ASO-capped AuNPs were mixed instead of all four (Au-ASO_{mix}). The choice of two of the ASO-capped AuNPs (either Au-ASO_{1M+2L} or Au-ASO_{3H+4M}) was based on their proximity to target one of the regions of *N* gene sequence. In all cases, it was observed that Au-ASO_{mix} was the optimum formulation to target SARS-CoV-2 RNA with higher sensitivity than the other sensors tested herein.

Interestingly, as per our hypothesis, the Au-ASO_{mix} nanoparticles were confirmed to be individually dispersed in the sample in absence of the viral load, which in the presence of SARS-CoV-2 RNA tend to agglomerate forming large clusters. The aggregation of AuNPs was confirmed from the increase in absorbance of the aggregation band at 660 nm^{51–53} when the Au-ASO_{mix} nanoparticles were exposed to a definite concen-

tration of total RNA (1 ng/μL) extracted from the Vero cells infected with SARS-CoV-2 with an incubation time of 15 min at room temperature. Table S1 represents a comparative overview of change in average hydrodynamic diameter (D_{ah}), as observed from Zetaview, and average size of the aggregated nanoparticles, as measured from the TEM analyses, for the Au-ASO_{mix} nanoparticle before and after addition of its target SARS-CoV-2 viral RNA. It was evident that there was minimal change in hydrodynamic diameters when the individual ASO-capped AuNPs were mixed with each other (Figure 2c). But the hydrodynamic diameter of Au-ASO_{mix} nanoparticles increased largely with the addition of its target RNA containing SARS-CoV-2 (Figure 4b). This indicated the enhanced propensity of the nanoparticles to aggregate in the presence of its target RNA containing SARS-CoV-2. The screenshots as observed from ZetaView are shown in Movie S2.

This response of Au-ASO_{mix} nanoparticles to its target viral RNA was further corroborated by the TEM images. A significant amount of clustering was found among the nanoparticles in the presence of their target viral RNA (Figure 4c–f). The formation of both large (~120 nm) and small (~80 nm) gold nanoparticle entities was observed in the sample. It was also monitored that the optimum sensitivity was achieved within 4–6 min of incubation at room temperature of the nanoparticles with the total RNA (1 ng/μL) extracted from the Vero cells infected with SARS-CoV-2 (Figure 4g). To further investigate the sensitivity of Au-ASO_{mix} and the selective agglomeration of the nanoparticles in the presence of the viral SARS-CoV-2 RNA, we visualized the particles under enhanced dark-field hyperspectral imaging microscope. The hyperspectral imaging (HSI) provided a label-free detection approach, combining both imaging and spectrophotometry, that can be used to localize nanomaterial based on their hyperspectral signature.⁵⁴ The HSI system utilizes advanced optics and computational algorithms to capture a spectrum from 400 to 1000 nm at each pixel of the image with an enhanced dark-field microscope (EDFM). The obtained spectrum represents a signature of each individual material that can be used to confirm the identity of the materials of interest in a mixture of the sample. This information can further be utilized to create an image “map” to reveal the presence and location of material of interest in the targeted sample. EDFM-HSI mapping thus proves to be an accurate technique that could locate and identify nanomaterials in samples more efficiently when compared to other conventional techniques.^{54,55}

Figure 5a illustrates the EDFM-HSI image of the Au-ASO_{mix} nanoparticles in the absence of its target SARS-CoV-2 RNA. Consistent with our previous results, the AuNPs in the Au-ASO_{mix} were found to be well dispersed with insignificant aggregation propensity among the AuNPs. Figure 5b shows the average spectrum of the hyperspectral signal of all the AuNPs that existed in the dark-field image (Figure S2). After the addition of the RNA having SARS-CoV-2 viral gene, a significant number of clustered gold nanoparticles were observed in the sample indicating the enhanced propensity among the nanoparticles to aggregate which is consistent with the previous TEM, Zetaview, and optical absorbance results (Figure 5c). The agglomeration propensity among the AuNPs in the presence of its target viral RNA can thus be related to the precise designing, targeting ability and binding affinity of the ASOs with their target gene. A significant change in the hyperspectral signature of the sample has been found where a

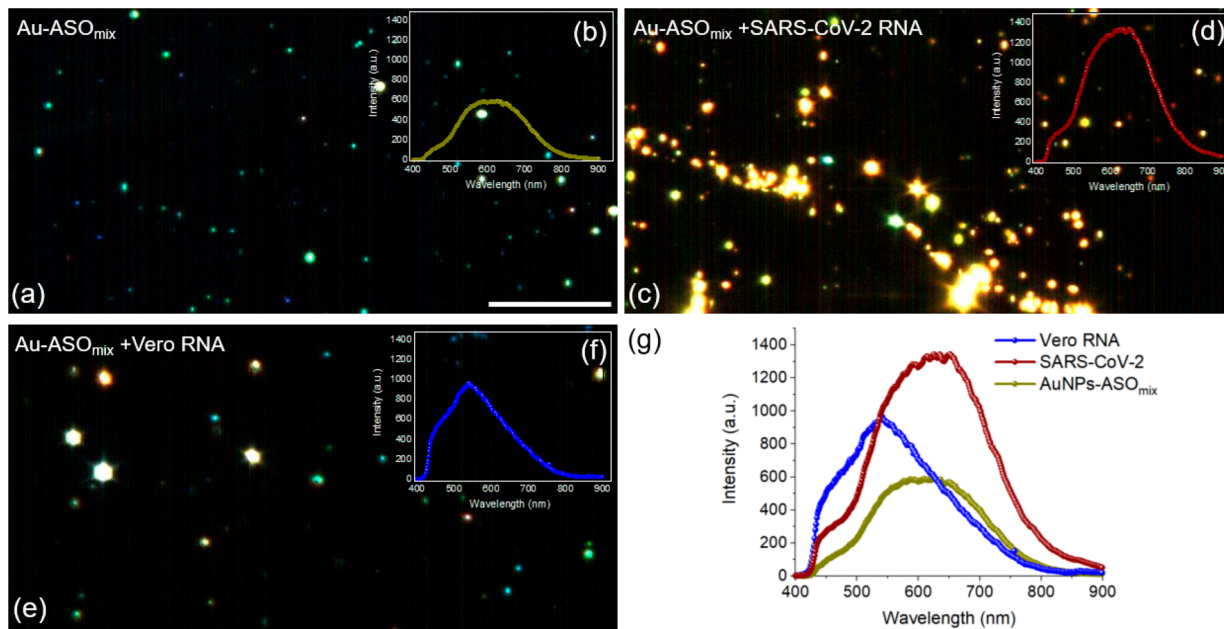


Figure 5. EDFM-HSI of the Au-ASO_{mix} (a) in the absence of RNA and in the presence of (c) RNA containing the viral SARS-CoV-2 gene and (e) control noninfected RNA from the Vero cells. The average of the hyperspectral data obtained from the Au-ASO_{mix} (b) in the absence of RNA and in the presence of (d) RNA containing the viral SARS-CoV-2 gene and (f) control noninfected RNA from the Vero cells. The overlay of hyperspectral data is represented in (g).

sharp peak has been observed after the addition of the viral RNA. Further, in the presence of the viral RNA we observed broadening in the average spectral signature with a redshift in the spectrum tail (Figures 5d and S2). Multiples of such hyperspectral images of Au-ASO_{mix} nanoparticles conjugated with SARS-CoV-2 RNA are represented in Figure S3 and Movie S3.

In addition, it is also fundamentally important to identify the distribution and location of each type of Au-ASOs in the hybrid cluster of Au-ASO_{mix} when bound with its target SARS-CoV-2 viral RNA. In order to receive this valuable information, the hyperspectral data of each individual Au-ASOs (i.e., Au-ASO_{1M}, Au-ASO_{2L}, Au-ASO_{3H}, and Au-ASO_{4M}) were recorded and stored in the spectral library for further analysis. Using these data, an image “map” was generated to identify the location of each individual Au-ASOs in the hybrid cluster. Figure 6 illustrates the mapping images of the Au-ASOs. It was observed that Au-ASO_{3H} has the highest distribution across the sample which was followed by Au-ASO_{4M}, Au-ASO_{1M}, and Au-ASO_{2L} (Figure S4) which might be a combinatorial effect of theoretical binding disruption energies, theoretical target binding energies (Table 1), and experimental sensing capabilities of each of the ASOs (Figure 3). Figure 6b–f depicts a zoomed-in image of the hybrid cluster of gold nanoparticles where the location of each of the Au-ASOs is represented using color code (red, green, blue, and purple). Interestingly, the nanoparticles Au-ASO_{1M} and Au-ASO_{2L} (red and green, respectively) were found to be localized in regions close to each other which is primarily due to the proximity of their target position in the N gene sequence of SARS-CoV-2, that is, the target position is 421–440 for ASO1 and 443–462 for ASO2 (Table 1), further assuring the hypothesis of the sensing mechanism.

The increase in sensitivity of Au-ASO_{mix} nanoparticles was also monitored at a definite concentration of RNA containing SARS-CoV-2 (1 ng/μL) with change in incubation temper-

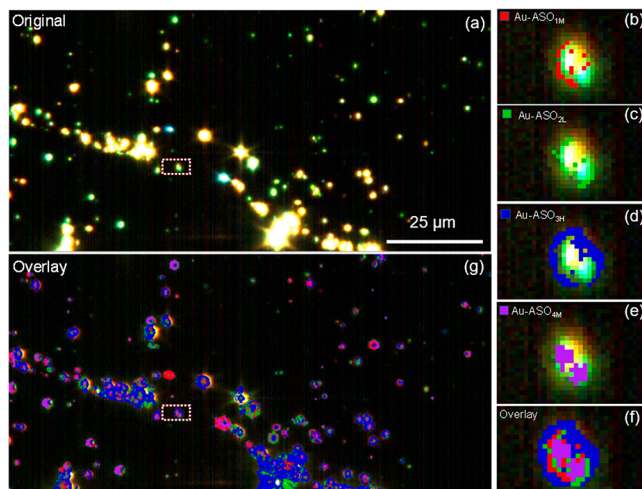


Figure 6. Hyperspectral map image of the Au-ASO_{mix} in the presence of the RNA of the SARS-CoV-2 virus (a) EDFM-HSI original image, (b) overlay of the image “map” on the EDFM-HSI image. (c–g) Zoom-in image in the dotted box of the AuNPs cluster showing the localization of (a) Au-ASO_{1M} (red), (b) Au-ASO_{2L} (green), (c) Au-ASO_{3H} (blue), (d) Au-ASO_{4M} (purple), and (f) overlay of the four Au-ASOs.

ature and it was observed that the optimum sensitivity was achieved at 37 °C (Figure S5). With this optimization, the change in absorbance of Au-ASO_{mix} at 660 nm was monitored with the increase in RNA concentrations while incubating each sample for 5 min at a constant temperature of 37 °C. A constant increase in absorbance with linear response was achieved which confirms the reliable and stable response of the Au-ASO_{mix} nanoparticle toward the SARS-CoV-2 RNA (Figure S6). The limit of detection was found to be 0.18 ng/μL with a tested dynamic range of 0.2–3 ng/μL. The analytical performance of Au-ASO_{mix} nanoparticles toward the detection

of viral SARS-CoV-2 RNA was further validated by comparing the relative limit of detection of different ASO-stabilized gold nanoparticles (**Figure S7**). The relatively low limit of detection in the case of Au-ASO_{mix} nanoparticles can be corroborated with the analytical sensitivity of differentially functionalized AuNPs (**Figure S1**). A prominent change in color of the solution from violet to dark blue was also observed after the addition of SARS-CoV-2 viral RNA load to the solution of Au-ASO_{mix} nanoparticles, and we tried to further improve its plasmonic signal response. Accordingly, we tried to amplify the signal response from the Au-ASO_{mix} nanoparticle with further deposition of more gold on the initially hybridized Au-ASO-RNA seeds.⁵⁶ A solution containing cetyltrimethylammonium bromide (CTAB) and ascorbic acid (AA) was then transferred to the already hybridized Au-ASO_{mix} nanoconjugate with SARS-CoV-2 RNA and mixed properly. Chloroauric acid (HAuCl₄) was then added to the mixture to initiate the chemical deposition process which amplified the signal response almost to an average of 75 times for the Au-ASO_{mix} nanoparticle within an incubation time of 30 min (**Figure S8**). The relative sensitivity of Au-ASO_{IM} was also compared with Au-ASO_{mix} nanoparticles.

Selectivity of Au-ASO_{mix} toward SARS-CoV-2. Another important parameter for any biosensor is the selectivity of the sensor toward its target. In this regard, the selectivity of the current SARS-CoV-2 sensor was tested when the Au-ASO_{mix} nanoparticle was treated against the total RNA isolated from cell lysate of Vero cells infected with MERS-CoV and the total RNA isolated from cell lysate of noninfected Vero cells. An insignificant change in absorbance at 660 nm wavelength (**Figure 7a**) was observed when the Au-ASO_{mix} nanoparticles were treated with these RNAs (1 ng/μL). Thus, both the RNAs extracted from noninfected Vero cells and Vero cells infected with MERS-CoV acted as negative controls for our

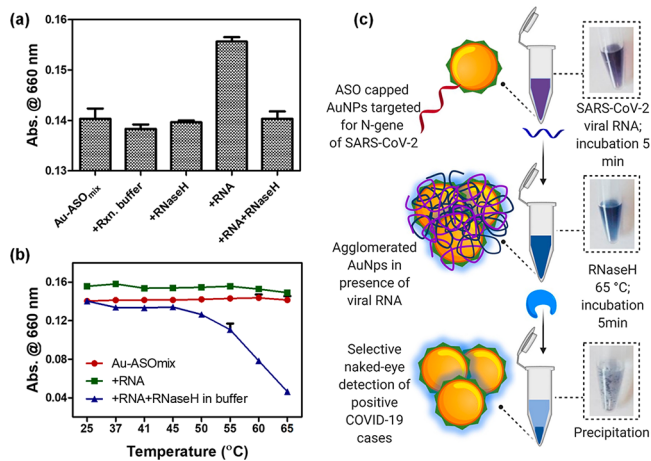


Figure 7. (a) Comparison of response of the Au-ASO_{mix} nanoparticles toward the RNA (1 ng/μL) isolated from noninfected Vero cells, Vero cells infected with MERS-CoV, and Vero cells infected with SARS-CoV-2 virus. Relative change in absorbance at 660 nm wavelength for the Au-ASO_{mix} nanoparticle treated with SARS-CoV-2 RNA (1 ng/μL) followed by the addition of RNase H has been plotted in (b) when the mixture was incubated at different temperatures for 5 min. The schematic representation for the visual naked-eye detection of SARS-CoV-2 with the treatment of RNase H at 65 °C for 5 min is shown in (c). The error bar indicates the average results obtained from three such independent experiments performed in triplicate.

experiments. Thus, the bioengineered ASO-capped gold nanoparticles, Au-ASO_{mix} could potentially be used for the selective detection of SARS-CoV-2. Further the selectivity of the Au-ASO_{mix} nanoparticle was also confirmed by the hyperspectral technique when the nanoparticles were treated with the RNA isolated from the noninfected Vero cells as a negative control. **Figure 5e** illustrates the EDFM-HSI of the Au-ASO_{mix} after the addition of the RNA isolated from the noninfected Vero cells. No obvious aggregates were observed in the presence of this RNA, which supports our hypothesis about the selectivity of the designed ASOs toward SARS-CoV-2. Insignificant change in hyperspectral signature was also evident from **Figures Sf** and **S1c**, further confirming the selectivity of the Au-ASO_{mix} nanoparticles toward SARS-CoV-2 viral RNA. Interestingly, a significant hyperspectral shift (~100 nm) was found for the Au-ASO_{mix} nanoparticles treated with RNA containing the viral SARS-CoV-2 gene (**Figure 5g**) confirming that the aggregation happens only in the presence of their target RNA containing the viral N gene of SARS-CoV-2. Thus, the enhanced dark-field microscopic images and the hyperspectral data confirmed the sensitivity and the selectivity of the developed platform in identifying the presence of COVID-19 causative virus, SARS-CoV-2, in the sample.

Visual Naked-Eye Detection of SARS-CoV-2. Further we intended to receive a marked change in visual appearance of the test solution in the presence of SARS-CoV-2 virus which could be easily detected even by a layman. During the previous set of experiments, an increase in absorbance at 660 nm wavelength with a redshift of ~40 nm was observed with a difference in color from violet to dark blue, but a marked change in visual appearance was desired to potentially be used for the detection of SARS-CoV-2.

In this regard, we thought of a bioassay with the addition of thermostable RNase H to the mixture containing Au-ASO_{mix} and total RNA having the SARS-CoV-2 gene. It has been envisaged that the thermostable RNase H will specifically recognize and cleave the phosphodiester bonds of the SARS-CoV-2 RNA (N gene) strand hybridized with the Au-ASO_{mix} nanoconjugate while leaving the ASO strands intact. It has been presumed that this treatment of RNase H may greatly influence the agglomeration propensity among the gold nanoparticles that are already hybridized along the RNA strand which might also fulfill our aim of achieving an immediate change in visual appearance of the solution. To our expectation, no change in absorbance at 660 nm from the base absorbance of Au-ASO_{mix} nanoparticle was observed when the hybridized Au-ASO_{mix} nanoconjugate with SARS-CoV-2 RNA was treated with RNase H with an incubation of 5 min at room temperature (**Figure S9**). A further decrease in absorbance was observed when the mixture was incubated at higher temperatures indicating the increased activity of RNase H at elevated temperature levels (**Figure 7b**). A marked change in visual appearance of the solution was achieved when the mixture was incubated at an elevated temperature of 65 °C for 5 min (**Figure S10**), which is schematically represented in **Figure 7c**. This phenomenon may therefore be explained from the activity of RNase H to selectively cleave the RNA strand from the RNA conjugate with Au-ASO_{mix} which leads to further agglomeration among the AuNPs those are attached to the RNA strand followed by precipitation of AuNPs from the solution. The test was also found to be selective to the presence of viral SARS-CoV-2 RNA load as the treatment of RNase H to the sample containing Au-ASO_{mix} and RNA from

Vero cells infected with MERS-CoV and caused no change in absorbance. Overall, this study reports the naked-eye detection of COVID-19 causative virus, SARS-CoV-2 within a minimal time frame of ~10 min from the total RNA derived from the virus infected cells.

Thus, the present study describes the isolation of total RNA from a biosample infected with the COVID-19 causative virus, SARS-CoV-2, and selective naked-eye detection of the virus mediated by suitably designed antisense oligonucleotide capped gold nanoparticles. The sensing mechanism initiates with the initial 5 min room temperature incubation of the RNA samples having the viral load with a composite of ASO-capped AuNPs which is followed by the treatment of RNase H at 65 °C for 5 min to generate a visual precipitate from the solution. Furthermore, the present method describes the selective naked-eye instrument-less detection of SARS-CoV-2 which can also be correlated with the concentration of viral RNA present in the sample as the assay relies on the target-induced aggregation and precipitation of the ASO-capped AuNPs. We have also compared the features of our COVID-19 biosensor with the competing commercially available FDA approved or under revision diagnostic approaches (Tables S2 and S3) and peer-reviewed articles published on diagnostic approaches (Table S4) and proposed a new design of SARS-CoV-2 diagnostic test that can selectively detect the presence of SARS-CoV-2 by naked-eye in a biospecimen without the requirement of any sophisticated instrument. The reliability of many diagnostic tests fail when they are tested either to a viral load at its early representation or to a viral gene mutated during its current spread, but our sensor design attempts to compensate for these drawbacks by directly targeting the *N* gene of SARS-CoV-2 simultaneously at multiple positions of the gene.

CONCLUSION

Briefly, we report herein the development of a colorimetric bioassay utilizing the efficient targeting and binding ability of the antisense oligonucleotides specific for *N*-gene of SARS-CoV-2 viral genome in conjugation with the anisotropic plasmonic properties of gold nanoparticles. The methodology, described herein, further utilizes an all-inclusive targeting approach mediated by four of the ASO sequences covering two regions of the viral genome sequence, that is, *N*-gene of SARS-CoV-2, at the same time. The gold nanoparticles when capped with the ASOs have been utilized for diagnosing positive COVID-19 cases within 10 min from the total RNA isolated from the infected biosamples. The thiol-modified ASO-capped AuNPs agglomerate selectively in the presence of its target RNA sequence of SARS-CoV-2 and demonstrate a change in its SPR with a redshift of ~40 nm in their absorbance spectra. The agglomeration of ASO-capped gold nanoparticles in the presence of SARS-CoV-2 RNA was studied by UV-visible absorbance spectroscopy, transmission electron microscopy, and hyperspectral microscopy. Further, the addition of RNase H cleaves the RNA strand from the composite hybrid of RNA and Au-ASO_{mix} leading to a visually detectable precipitate from the solution mediated by the additional agglomeration among the AuNPs. The selectivity of this COVID-19 biosensor has also been tested against MERS-CoV viral RNA load where no distinct change in absorbance was found with MERS-CoV RNA. Thus, the current study reports a reliable, reproducible, selective, and visual naked-eye detection of COVID-19 causative virus, SARS-CoV-2 which is devoid of the require-

ment of any sophisticated instrumental techniques. In addition to this, the current methodology ensures its feasibility even with the mutated *N* gene forms of the virus during its spread as the assay has been designed to simultaneously target two separate regions of the gene. We also complied our SARS-CoV-2 specific sensor with the ASSURED criteria, mentioned by WHO, where the biosensor should have the following characteristics of (i) Affordable, (ii) Sensitive, (iii) Specific, (iv) User-friendly, (v) Rapid and robust, (vi) sophisticated Equipment-free, and (vii) Delivered to the end-users. Furthermore, the developed colorimetric bioassay could be modified to target other regions of the viral genomic material, such as *S*-gene (surface glycoprotein), *E*-gene (envelope protein) and *M*-gene (membrane glycoprotein), for potential preclinical screening and high sensitivity with minimal false positives.

MATERIALS AND METHODS

Materials. All of the chemicals were purchased from reputable commercial vendors and used without any further purification steps. The custom designed and thiol-modified ASOs were procured from GenScript and stored at -20 °C. All the experiments were carried out at constant room temperature of 25 °C unless otherwise specified. The Vero cells were procured from ATCC (Vero E6; ATCC CRL-1586). The gamma-irradiated cell lysate and supernatant from Vero E6 cells infected with SARS-CoV-2, isolate USA-WA1/2020, and Middle East Respiratory Syndrome Coronavirus (MERS-CoV), EMC/2012 was obtained from BEI Resources, NIAID, NIH. Thermostable RNase H was purchased from New England Biolabs.

Antisense Oligonucleotide Design. The target *N*-gene sequence of SARS-CoV-2, as mentioned in the Supporting Information, was supplied to a software for statistical folding of nucleic acids, and studies of regulatory RNAs, Soligo,⁵⁷ and the ASOs were predicted maintaining the folding temperature as 37 °C and ionic conditions of 1 M sodium chloride for a preferred length of ASO as 20 nucleotide bases. The filter criteria were set as follows:

- 1 $40\% \leq GC\% \leq 60\%$.
- 2 Elimination of target sequences with GGGG.
- 3 Average unpaired probability of the ASOs for target site nucleotides to be ≥ 0.5 .
- 4 Considering the threshold probability of above 0.5, all sites targeted to the peak in the accessibility profile are ranked by their average unpaired probability (the higher the better);
- 5 Among sites satisfying criteria 1–4, the top 20 ones with the highest average unpaired probability will be considered. The average unpaired probability was also used in filter criteria 3, 4, and 5 to reduce the number of reported sites in order to optimize the disruption energy calculation in the web servers.
- 6 Further, the binding energy of the ASOs were also compared with the target sequence where the binding energy cutoff for the selection of ASOs was kept at ≤ -8 kcal/mol.

Synthesis of Citrate-Stabilized Gold Nanoparticles. A solution of 2.2 mM of sodium citrate was taken in Milli-Q water (150 mL) and refluxed for 15 min under vigorous stirring. A solution of 1 mL of HAuCl₄ (25 mM) was injected to the boiling solution of sodium citrate. The color of the solution changed over a time period of 20 min. The resulting citrate-capped gold nanoparticles (AuNPs) were well suspended in H₂O.⁵⁸

Functionalization of AuNPs with ASOs. Citrate-stabilized AuNPs were taken at $\sim 3 \times 10^{10}$ particles/mL concentration as observed through zetaview software and treated with ASOs at three different concentrations, that is, 0.5, 1, and 2 μM from a stock of 200 μM for each of the four ASOs. The mixture was stirred at room temperature for 30 min, centrifuged to remove any excess of uncapped ASO from the supernatant, and the pellet was then resuspended in a similar volume of Milli-Q water. Accordingly, 12 different samples for four of the ASOs at three different

concentrations were prepared and nomenclatured as Au-ASO_{xL}, Au-ASO_{xM}, and Au-ASO_{xH} where x defines the number of ASO as 1, 2, 3, or 4 and L, M and H are representative of low, medium and high concentrations of ASOs respectively. The nanoparticles were kept at 4 °C for future use.

Cell Culture. The *Cercopithecus aethiops* kidney epithelial cells (Vero E6) were procured from ATCC (CRL-1586) and cultured at standard conditions in Eagle's Minimum Essential Medium with the supplement of 10% fetal bovine serum at 37 °C. The cells were trypsinized with 0.25% (w/v) Trypsin- 0.53 mM EDTA solution while maintaining the culture.

Isolation of RNA. Severe acute respiratory syndrome-related coronavirus (SARS-CoV-2), isolate USA-WA1/2020 was isolated from an oropharyngeal swab of a patient with a respiratory illness. The patient had returned from travel to the affected region of China and had developed clinical disease (COVID-19) in January 2020 in Washington, U.S.A. The sample, NR-52287, as obtained from BEI Resources, NIAID, NIH, consists of a crude preparation of cell lysate and supernatant from *Cercopithecus aethiops* kidney epithelial cells (Vero E6; ATCC CRL-1586) infected with severe acute respiratory syndrome-related coronavirus 2 (SARS-CoV-2), isolate USA-WA1/2020 that was gamma-irradiated (5×10^6 RADs) on dry ice. The sample, NR-50549, as obtained from BEI Resources, NIAID, NIH, consists of a gamma-irradiated cell lysate and supernatant from Vero cells infected with MERS-CoV, EMC/2012. This sample was isolated from a man with pneumonia in Saudi Arabia.

The Vero cells with or without the viral transfection were lysed directly in a culture dish by adding 1 mL of TRIzol reagent and aspirated carefully. The total RNA was then extracted and purified for the viral RNA from the cellular lysate with a commercially available kit. The concentration of purified RNA, isolated from the SARS-CoV-2 infected Vero cells, was found to be 35.9 ng/μL, while the concentration of the purified RNA, isolated from the noninfected Vero cells, was 92.6 ng/μL.

Sample Standardization Protocol. The as-synthesized nanoparticles were taken out from the refrigerator, sonicated for 5 min in a bath sonicator (Branson 2800) at room temperature, and vortexed for 2 min prior use. To determine the sensing capability of the individually ASO-capped gold nanoparticles, the as-synthesized solution containing the AuNPs were treated with RNA samples having the concentration of 1 ng/μL. For the preparation of each 100 μL of Au-ASO_{mix}, 25 μL of each individual Au-ASO_{1L}, Au-ASO_{2L}, Au-ASO_{3H}, and Au-ASO_{4M} nanoparticles were mixed and vortexed thoroughly. The sensing and targeting capability of the Au-ASO_{mix} was also validated at a RNA concentration of 1 ng/μL.

Protocol for Signal Amplification. The signal amplification was investigated following a literature reported protocol.⁵⁴ Briefly, 100 μL solution of Au-ASO_{mix} was first treated with RNA containing SARS-CoV-2 at a concentration of 1 ng/μL. This solution was then incubated with CTAB, L-ascorbic acid, and HAuCl₄ at a concentration of 0.1 M, 0.45 mM, and 0.225 mM, respectively, and monitored over several time points.

Protocol for RNase H Treatment. For each 100 μL of reaction, 10 μL of RNase H reaction buffer (1X) was used along with 1 μL of thermostable RNase H and incubated for a required time at a definite temperature. The 100 μL solution of Au-ASO_{mix} nanoparticle was first treated with RNA samples having 1 ng/μL concentration and then incubated with RNase H reaction buffer (1X) and thermostable RNase H for required time points and temperature.

Absorbance Spectra. The absorbance spectra were initially acquired on a VWR UV-vis spectrophotometer, while the assays with 96-well plates were monitored on Bioktek Synergy Neo2Microplate Reader both for end point, kinetic, and spectral analyses.

Measurement of Hydrodynamic Diameter. The hydrodynamic diameters of the individually ASO-capped gold nanoparticles and the composite nanoparticles (Au-ASO_{mix}) were monitored on a particle tracking analyzer (Zetaview Particle Metrix). The hydrodynamic diameters of Au-ASO_{mix} before and after the addition of RNA at a concentration of 1 ng/μL were also observed in a similar fashion. The as-synthesized nanoparticles were diluted 50 times and 1

mL of such diluted samples were injected into the machine for the measurements. The chamber of the machine was properly cleaned prior to each measurement.

Transmission Electron Microscopy. The as-synthesized nanoparticles, Au-ASO_{mix} before and after the addition of RNA at a concentration of 1 ng/μL, were investigated under the transmission electron microscope (FEI tecna T12). The tungsten filament was used as the electron optics, and the voltage was kept constant at 80 kV. A 20 μL sample droplet was spotted onto a carbon-coated copper grid (400 mesh) and allowed to stay there for about 10 min before being removed.

Hyperspectral Analyses. The as-synthesized nanoparticles, Au-ASO_{mix} before and after the addition of RNA at a concentration of 1 ng/μL, were also monitored under the dark-field optical microscope (CytoViva), and their hyperspectra were acquired by the hyperspectral recorder from CytoViva. The hyperspectra were compared for the Au-ASO_{mix} nanoparticles when treated with the RNA isolated from the Vero cells with or without transfected with SARS-CoV-2 separately. A 20 μL sample droplet was spotted onto a glass slide and a coverslip was placed on top of it.

ASSOCIATED CONTENT

Supporting Information

The following files are available online free of charge: N-gene sequence, figure S1–S10, movie S1–S3, table S1–S4 and supporting references. The Supporting Information is available free of charge at <https://pubs.acs.org/doi/10.1021/acsnano.0c03822>.

(PDF)

Screenshots of Au-ASO_{mix} nanoparticles as observed through zetaview ([MP4](#))

Screenshots of Au-ASO_{mix} nanoparticles as observed through zetaview after the addition of total RNA (1 ng/μL) isolated from the Vero cells infected with SARS-CoV-2 ([MP4](#))

The movement of agglomerated Au-ASO_{mix} nanoparticles as a string in presence of SARS-CoV-2 RNA ([MP4](#))

AUTHOR INFORMATION

Corresponding Author

Dipanjan Pan — Departments of Diagnostic Radiology and Nuclear Medicine and Pediatrics, Center for Blood Oxygen Transport and Hemostasis, University of Maryland Baltimore School of Medicine, Baltimore, Maryland 21201, United States; Bioengineering Department, University of Illinois at Urbana-Champaign, Urbana, Illinois 61801, United States; Department of Chemical, Biochemical, and Environmental Engineering, University of Maryland Baltimore County, Baltimore, Maryland 21250, United States;  orcid.org/0000-0003-0175-4704; Email: dipanjan@som.umaryland.edu

Authors

Parikshit Moitra — Departments of Diagnostic Radiology and Nuclear Medicine and Pediatrics, Center for Blood Oxygen Transport and Hemostasis, University of Maryland Baltimore School of Medicine, Baltimore, Maryland 21201, United States;  orcid.org/0000-0002-7679-7859

Maha Alafeef — Departments of Diagnostic Radiology and Nuclear Medicine and Pediatrics, Center for Blood Oxygen Transport and Hemostasis, University of Maryland Baltimore School of Medicine, Baltimore, Maryland 21201, United States; Bioengineering Department, University of Illinois at Urbana-Champaign, Urbana, Illinois 61801, United States;

Biomedical Engineering Department, Jordan University of Science and Technology, Irbid 22110, Jordan

Ketan Dighe – Department of Chemical, Biochemical, and Environmental Engineering, University of Maryland Baltimore County, Baltimore, Maryland 21250, United States

Matthew B. Frieman – Department of Microbiology and Immunology, University of Maryland School of Medicine, Baltimore, Maryland 21201, United States

Complete contact information is available at:

<https://pubs.acs.org/10.1021/acsnano.0c03822>

Author Contributions

#P.M. and M.A. contributed equally to this work.

Author Contributions

The manuscript was written through contributions of all authors. All authors have given approval to the final version of the manuscript.

Notes

The authors declare the following competing financial interest(s): Prof Pan is the founder or co-founder of three University based start ups. None of these entities however, supported this work.

ACKNOWLEDGMENTS

Authors gratefully acknowledge the receipt of funding from University of Maryland Baltimore and University of Maryland Baltimore County. The following reagents were deposited by the Centers for Disease Control and Prevention and obtained through BEI Resources, NIAID, NIH: (i) SARS-Related Coronavirus 2, Isolate USA-WA1/2020, Gamma-Irradiated, NR-52287 and (ii) Middle East Respiratory Syndrome Coronavirus (MERS CoV), EMC/2012, Irradiated Infected Cell Lysate, NR-50549.

REFERENCES

- (1) Huang, C.; Wang, Y.; Li, X.; Ren, L.; Zhao, J.; Hu, Y.; Zhang, L.; Fan, G.; Xu, J.; Gu, X.; Cheng, Z.; Yu, T.; Xia, J.; Wei, Y.; Wu, W.; Xie, X.; Yin, W.; Li, H.; Liu, M.; Xiao, Y.; Gao, H.; Guo, L.; Xie, J.; Wang, G.; Jiang, R.; Gao, Z.; Jin, Q.; Wang, J.; Cao, B. Clinical Features of Patients Infected with 2019 Novel Coronavirus in Wuhan, China. *Lancet* **2020**, *395*, 497–506.
- (2) Velavan, T. P.; Meyer, C. G. The Covid-19 Epidemic. *Trop. Med. Int. Health* **2020**, *25*, 278–280.
- (3) Phan, T. Genetic Diversity and Evolution of Sars-Cov-2. *Infect. Genet. Evol.* **2020**, *81*, 104260.
- (4) Sun, Fu.; Ganguli, A.; Nguyen, J.; Brisbin, R.; Shanmugam, K.; Hirschberg, D. L.; Wheeler, M. B.; Bashir, R.; Nash, D. M.; Cunningham, B. T. Smartphone-Based Multiplex 30-minute Nucleic Acid Test of Live Virus from Nasal Swab Extract. *Lab Chip* **2020**, *20*, 1621–1627.
- (5) Wu, F.; Zhao, S.; Yu, B.; Chen, Y. M.; Wang, W.; Song, Z. G.; Hu, Y.; Tao, Z. W.; Tian, J. H.; Pei, Y. Y.; Yuan, M. L.; Zhang, Y. L.; Dai, F. H.; Liu, Y.; Wang, Q. M.; Zheng, J. J.; Xu, L.; Holmes, E. C.; Zhang, Y. Z. A New Coronavirus Associated with Human Respiratory Disease in China. *Nature* **2020**, *579*, 265–269.
- (6) Coronaviridae Study Group of the International Committee on Taxonomy of Viruses.. The Species Severe Acute Respiratory Syndrome-Related Coronavirus: Classifying 2019-nCoV and Naming It SARS-CoV-2. *Nat. Microbiol.* **2020**, *5*, S36–S44.
- (7) de Wit, E.; van Doremalen, N.; Falzarano, D.; Munster, V. J. SARS and MERS: Recent Insights into Emerging Coronaviruses. *Nat. Rev. Microbiol.* **2016**, *14*, S23–S34.
- (8) Lu, R.; Zhao, X.; Li, J.; Niu, P.; Yang, B.; Wu, H.; Wang, W.; Song, H.; Huang, B.; Zhu, N.; Bi, Y.; Ma, X.; Zhan, F.; Wang, L.; Hu, T.; Zhou, H.; Hu, Z.; Zhou, W.; Zhao, L.; Chen, J.; et al. Genomic Characterisation and Epidemiology of 2019 Novel Coronavirus: Implications for Virus Origins and Receptor Binding. *Lancet* **2020**, *395*, S65–S74.
- (9) Li, Q.; Guan, X.; Wu, P.; Wang, X.; Zhou, L.; Tong, Y.; Ren, R.; Leung, K. S. M.; Lau, E. H. Y.; Wong, J. Y.; Xing, X.; Xiang, N.; Wu, Y.; Li, C.; Chen, Q.; Li, D.; Liu, T.; Zhao, J.; Liu, M.; Tu, W.; et al. Early Transmission Dynamics in Wuhan, China, of Novel Coronavirus-Infected Pneumonia. *N. Engl. J. Med.* **2020**, *382*, 1199–1207.
- (10) Guan, W.; Ni, Z.; Hu, Y.; Liang, W.; Ou, C.; He, J.; Liu, L.; Shan, H.; Lei, C.; Hui, D. S. C.; Du, B.; Li, L.; Zeng, G.; Yuen, K.-Y.; Chen, R.; Tang, C.; Wang, T.; Chen, P.; Xiang, J.; Li, S. Clinical Characteristics of 2019 Novel Coronavirus Infection in China. *N. Engl. J. Med.* **2020**, *382*, 1708.
- (11) Yang, Y.; Lu, Q.; Liu, M.; Wang, Y.; Zhang, A.; Jalali, N.; Dean, N.; Longini, I.; Halloran, M. E.; Xu, B.; Zhang, X.; Wang, L.; Liu, W.; Fang, L. Epidemiological and Clinical Features of the 2019 Novel Coronavirus Outbreak in China. *medRxiv* **2020** DOI: [10.1101/2020.02.10.202021675](https://doi.org/10.1101/2020.02.10.202021675) (accessed May 4, 2020).
- (12) Huang, H.; Fan, C.; Li, M.; Nie, H.-L.; Wang, F.-B.; Wang, H.; Wang, R.; Xia, J.; Zheng, X.; Zuo, X.; Huang, J. COVID-19: A Call for Physical Scientists and Engineers. *ACS Nano* **2020**, *14*, 3747–3754.
- (13) Ferguson, N.; Laydon, D.; Nedjati-Gilani, G.; Imai, N.; Ainslie, K.; Baguelin, M.; Bhatia, S.; Boonyasiri, A.; Cucunubá, P. Z.; Cuomo-Dannenburg, G.; Dighe, A.; Dorigatti, I.; Fu, H.; Gaythorpe, K.; Green, W.; Hamlet, A.; Hinsley, W.; Okell, L.; Van Elsland, S.; Thompson, H., et al. Report 9: Impact of Non-Pharmaceutical Interventions (NPIs) to Reduce COVID-19 Mortality and Healthcare Demand; Imperial College London: London, 2020; pp 1–20.
- (14) Prem, K.; Liu, Y.; Russell, T. W.; Kucharski, A. J.; Eggo, R. M.; Davies, N.; Flasche, S.; Clifford, S.; Pearson, C. A. B.; Munday, J. D.; Abbott, S.; Gibbs, H.; Rosello, A.; Quilty, B. J.; Jombart, T.; Sun, F.; Diamond, C.; Gimma, A.; van Zandvoort, K.; Funk, S.; Jarvis, C. I.; Edmunds, W. J.; Bosse, N. I.; Hellewell, J.; Jit, M.; Klepac, P. The Effect of Control Strategies to Reduce Social Mixing on Outcomes of the COVID-19 Epidemic in Wuhan, China: A Modelling Study. *Lancet Public Health* **2020**, *5*, E261–E270.
- (15) Normalie, D. Coronavirus Cases Have Dropped Sharply in South Korea. What's the Secret to Its Success? <https://www.sciencemag.org/news/2020/03/coronavirus-cases-have-dropped-sharply-south-korea-whats-secret-its-success>. March 17, 2020 (accessed May 4, 2020).
- (16) Colbourne, T. COVID-19: Extending or Relaxing Distancing Control Measures. *Lancet Public Health* **2020**, *5*, E236–E237.
- (17) Rahimi, F.; Talebi Bezmin Abadi, A. Practical Strategies against the Novel Coronavirus and COVID-19 — The Imminent Global Threat. *Arch. Med. Res.* **2020**, *51*, 280.
- (18) Rodriguez-Morales, A. J.; MacGregor, K.; Kanagarajah, S.; Patel, D.; Schlagenhauf, P. Going Global - Travel and the 2019 Novel Coronavirus. *Travel Med. Infect. Dis.* **2020**, *33*, 101578.
- (19) Dhami, K.; Sharun, K.; Tiwari, R.; Sircar, S.; Bhat, S.; Malik, Y. S.; Singh, K. P.; Chaicumpa, W.; Bonilla-Aldana, D. K.; Rodriguez-Morales, A. J. Coronavirus Disease 2019 – COVID-19. *Preprints* **2020**, 2020030001 (accessed May 4, 2020).
- (20) Ai, T.; Yang, Z.; Hou, H.; Zhan, C.; Chen, C.; Lv, W.; Tao, Q.; Sun, Z.; Xia, L. Correlation of Chest CT and RT-PCR Testing in Coronavirus Disease 2019 (Covid-19) in China: A Report of 1014 Cases. *Radiology* **2020**, 200642.
- (21) Kim, H. Outbreak of Novel Coronavirus (Covid-19): What Is the Role of Radiologists? *Eur. Radiology* **2020** DOI: [10.1007/s00330-020-06748-2](https://doi.org/10.1007/s00330-020-06748-2), (accessed May 4, 2020).
- (22) Wang, W.; Xu, Y.; Gao, R.; Lu, R.; Han, K.; Wu, G.; Tan, W. Detection of SARS-CoV-2 in Different Types of Clinical Specimens. *JAMA* **2020**, *323*, 1843–1844.
- (23) Carter, L. J.; Garner, L. V.; Smoot, J. W.; Li, Y.; Zhou, Q.; Saveson, C. J.; Sasso, J. S.; Gregg, A. C.; Soares, D. J.; Beskid, T. R.; Jersey, S. R.; Liu, C. Assay Techniques and Test Development for COVID-19 Diagnosis. *ACS Cent. Sci.* **2020**, *6*, S91–S05.

- (24) Yu, L.; Wu, S.; Hao, X.; Dong, X.; Mao, L.; Pelechano, V.; Chen, W.-H.; Yin, X. Rapid Detection of COVID-19 Coronavirus Using a Reverse Transcriptional Loop-Mediated Isothermal Amplification (RT-LAMP) Diagnostic Platform, *Clin. Chem.* **2020**, hvaa102.
- (25) Centers for Disease Control and Prevention. Real-Time RT-PCR Panel for Detection 2019-nCoV (US Centers for Disease Control and Prevention, 2020); <https://www.cdc.gov/coronavirus/2019-ncov/lab/rt-pcr-detection-instructions.html> (accessed May 1, 2020).
- (26) Udugama, B.; Kadhiresan, P.; Kozlowski, H. N.; Malekjahani, A.; Osborne, M.; Li, V. Y. C.; Chen, H.; Mubareka, S.; Gubbay, J. B.; Chan, W. C. W. Diagnosing COVID-19: The Disease and Tools for Detection. *ACS Nano* **2020**, *14*, 3822–3835.
- (27) Chan, W. C. W. Nano Research for COVID-19. *ACS Nano* **2020**, *14*, 3719–3720.
- (28) Pan, D.; Schirra, C. O.; Wickline, S. A.; Lanza, G. M. Multicolor Computed Tomographic Molecular Imaging with Noncrystalline High-Metal-Density Nanobeacons. *Contrast Media Mol. Imaging* **2014**, *9*, 13–25.
- (29) Pan, D.; Pramanik, M.; Senpan, A.; Yang, X.; Song, K. H.; Scott, M. J.; Zhang, H.; Gaffney, P. J.; Wickline, S. A.; Wang, L. V.; Lanza, G. M. Molecular Photo Acoustic Imaging (PAI) with Ligand-Directed Gold Nanobeacons. *Angew. Chem., Int. Ed.* **2009**, *48*, 4170–4173.
- (30) Pan, D.; Pramanik, M.; Senpan, A.; Ghosh, S.; Wickline, S. A.; Wang, L. V.; Lanza, G. M. Near Infrared Photoacoustic Detection of Sentinel Lymphnodes with Gold Nanobeacons. *Biomaterials* **2010**, *31*, 4088–4093.
- (31) Pan, D.; Pramanik, M.; Senpan, A.; Wickline, S. A.; Wang, L. V.; Lanza, G. M. A Facile Synthesis of Novel Self-Assembled Gold Nanorods Designed for Near-Infrared Imaging. *J. Nanosci. Nanotechnol.* **2010**, *10*, 8118–8123.
- (32) Pan, D.; Pramanik, M.; Senpan, A.; Stacy, A.; Zhang, H.; Wickline, S. A.; Wang, L. V.; Lanza, G. M. Molecular Photoacoustic Imaging of Angiogenesis with Integrin Targeted Gold Nanobeacons. *FASEB J.* **2011**, *25*, 875–882.
- (33) Zeng, J.; Zhang, Y.; Zeng, T.; Aleisa, R.; Qiu, Z.; Chen, Y.; Huang, J.; Wang, D.; Yan, Z.; Yin, Y. Anisotropic Plasmonic Nanostructures for Colorimetric Sensing. *Nano Today* **2020**, *32*, 100855.
- (34) Fraire, J. C.; Perez, L. A.; Coronado, E. A. Rational Design of Plasmonic Nanostructures for Biomolecular Detection: Interplay between Theory and Experiments. *ACS Nano* **2012**, *6*, 3441–3452.
- (35) Saha, K.; Agasti, S. S.; Kim, C.; Li, X.; Rotello, V. M. Gold Nanoparticles in Chemical and Biological Sensing. *Chem. Rev.* **2012**, *112*, 2739–2779.
- (36) Misra, S. K.; Dighe, K.; Schwartz-Duval, A. S.; Shang, Z.; Labriola, L. T.; Pan, D. *In Situ* Plasmonic Generation in Functional Ionic-Gold-Nanogel Scaffold for Rapid Quantitative Bio-Sensing. *Biosens. Bioelectron.* **2018**, *120*, 77–84.
- (37) Li, Z.; Askim, J. R.; Suslick, K. S. The Optoelectronic Nose: Colorimetric and Fluorometric Sensor Arrays. *Chem. Rev.* **2019**, *119*, 231–292.
- (38) Curry, T.; Kopelman, R.; Shilo, M.; Popovtzer, R. Multifunctional Theranostic Gold Nanoparticles for Targeted CT Imaging and Photothermal Therapy. *Contrast Media Mol. Imaging* **2014**, *9*, 53–61.
- (39) Peng, L.; Li, B. L.; Zhou, C. W.; Li, N. B.; Setyawati, M. I.; Zou, H. L. Naked-Eye Recognition: Emerging Gold Nano-Family for Visual Sensing. *Appl. Mater. Today* **2018**, *11*, 166–188.
- (40) Mirkin, C. A.; Letsinger, R. L.; Mucic, R. C.; Storhoff, J. J. A DNA-Based Method for Rationally Assembling Nanoparticles into Macroscopic Materials. *Nature* **1996**, *382*, 607–609.
- (41) Elghanian, R.; Storhoff, J. J.; Mucic, R. C.; Letsinger, R. L.; Mirkin, C. A. Selective Colorimetric Detection of Polynucleotides Based on the Distance-Dependent Optical Properties of Gold Nanoparticles. *Science* **1997**, *277*, 1078–1081.
- (42) Jung, Y. L.; Jung, C.; Parab, H.; Li, T.; Park, H. G. Direct Colorimetric Diagnosis of Pathogen Infections by Utilizing Thiol-Labeled PCR Primers and Unmodified Gold Nanoparticles. *Biosens. Bioelectron.* **2010**, *25*, 1941–1946.
- (43) Li, H.; Rothberg, L. J. Label-Free Colorimetric Detection of Specific Sequences in Genomic DNA Amplified by the Polymerase Chain Reaction. *J. Am. Chem. Soc.* **2004**, *126*, 10958–10961.
- (44) Li, H.; Rothberg, L. Colorimetric Detection of DNA Sequences Based on Electrostatic Interactions with Unmodified Gold Nanoparticles. *Proc. Natl. Acad. Sci. U. S. A.* **2004**, *101*, 14036–14039.
- (45) Shokri, E.; Hosseini, M.; Davari, M. D.; Ganjali, M. R.; Peppelenbosch, M. P.; Rezaee, F. Disulfide-Induced Self-Assembled Targets. A Novel Strategy for the Label Free Colorimetric Detection of DNAs/RNAs via Unmodified Gold Nanoparticles. *Sci. Rep.* **2017**, *7*, 1.
- (46) Kim, H.; Park, M.; Hwang, J.; Kim, J. H.; Chung, D.-R.; Lee, K.-S.; Kang, M. Development of Label Free Colorimetric Assay for MERS-CoV Using Gold Nanoparticles. *ACS Sens.* **2019**, *4*, 1306–1312.
- (47) Kalantar-Zadeh, K.; Ward, S. A.; Kalantar-Zadeh, K.; El-Omar, E. M.; Considering the Effects of Microbiome and Diet on SARS-CoV-2 Infection: Nanotechnology Roles, *ACS Nano* **2020** (in press) DOI: [10.1021/acsnano.0c03402](https://doi.org/10.1021/acsnano.0c03402).
- (48) Kostarelos, K. Nanoscale Nights of COVID-19. *Nat. Nanotechnol.* **2020**, *15*, 343–344.
- (49) Sportelli, M. C.; Izzi, M.; Kukushkina, E. A.; Hossain, S. I.; Picca, R. A.; Ditaranto, N.; Ciolfi, N. Can Nanotechnology and Materials Science Help the Fight against SARS-CoV-2? *Nanomaterials* **2020**, *10*, 802.
- (50) Bellino, M. G.; Calvo, E. J.; Gordillo, G. Adsorption Kinetics of Charged Thiols on Gold Nanoparticles. *Phys. Chem. Chem. Phys.* **2004**, *6*, 424–428.
- (51) Kim, D.-Y.; Shinde, S.; Saratale, R.; Syed, A.; Ameen, F.; Ghodake, G. Spectrophotometric Determination of Fe (III) by Using Casein-Functionalized Gold Nanoparticles. *Microchim. Acta* **2017**, *184*, 4695–4704.
- (52) Iglesias, E.; Prado-Gotor, R. Interaction of Gold Nanoparticles Mediated by Captopril and S-Nitrosocaptopril: The Effect of Manganese Ions in Mild Acid Medium. *Phys. Chem. Chem. Phys.* **2015**, *17*, 6444–654.
- (53) Chiu, N. F.; Chen, C. C.; Yang, C. D.; Kao, Y. S.; Wu, W. R. Enhanced Plasmonic Biosensors of Hybrid Gold Nanoparticle-Graphene Oxide-Based Label-Free Immunoassay. *Nanoscale Res. Lett.* **2018**, *13*, 152.
- (54) Misra, S. K.; Ostadhossein, F.; Daza, E.; Johnson, E. V.; Pan, D. Hyperspectral Imaging Offers Visual and Quantitative Evidence of Drug Release from Zwitterionic-Phospholipid-Nanocarbon When Concurrently Tracked in 3D Intracellular Space. *Adv. Funct. Mater.* **2016**, *26*, 8031.
- (55) Schwartz-Duval, A. S.; Misra, S. K.; Mukherjee, P.; Johnson, E.; Acerbo, A. S.; Pan, D. An Anisotropic Propagation Technique for Synthesizing Hyperbranched Polyvilllic Gold Nanoparticles. *Nano Res.* **2016**, *9*, 2889–2903.
- (56) Bai, X.; Shao, C. Y.; Han, X. G.; Li, Y. L.; Guan, Y. F.; Deng, Z. X. Visual Detection of Sub-Femtomole DNA by a Gold Nanoparticle Seeded Homogeneous Reduction Assay: Toward a Generalized Sensitivity-Enhancing Strategy. *Biosens. Bioelectron.* **2010**, *25*, 1984–1988.
- (57) Ding, Y.; Chan, C. Y.; Lawrence, C. E. Sfold Web Server for Statistical Folding and Rational Design of Nucleic Acids. *Nucleic Acids Res.* **2004**, *32*, W135–W141.
- (58) Bastús, N. G.; Comenge, J.; Puntes, V. Kinetically Controlled Seeded Growth Synthesis of Citrate-Stabilized Gold Nanoparticles of up to 200 nm: Size Focusing versus Ostwald Ripening. *Langmuir* **2011**, *27*, 11098–11105.